MATERIALS SCIENCES

Magnetism

X-Ray Scattering

In recent years, synchrotron radiation has become an important technique for the study of magnetic properties of thin films and surfaces. Recent examples include magnetic diffraction measurements by M. Conover *et al.* (U. of Illinois @ Urbana-Champagne), on X22C studying the influence of monolayer superlattice doping of rare earth metal films: Dy in Ho and Y in Er. They found that the imposed superlattice produced significant changes in the magnetic lock-in structure relative to bulk samples. On the same beamline, Helgesen studied the magnetic and structural properties of Er films grown epitaxially on Lu and Y, producing, respectively, compressed and expanded lattices relative to bulk Er. The depth profile of the magnetization was measured directly in a study of the magnetic disorder at the surface of a crystal of UO_2 by G. Watson *et al.* (U. of Maryland), on beamlines X22C and X25. Using X22C, A. Hiess *et al.* (EITU), found that thin films of the heavy fermion superconductor UPd_2Al_3 do not develop long range magnetic order, in contrast to bulk samples, and attributed that fact to the restricted dimensionality.

X-ray techniques continue to prove their importance in the determination of magnetic structures. Several recent experiments at beamline X22C include a determination of the magnetization of different lattice sites in (magnetically incommensurate) Nd by G. Watson *et al.* (U. of Maryland), the use of resonant exchange scattering to find the magnetic moment directions in $SmNi_2B_2C$ and $NdNi_2B_2C$ (C. Detlefs, *et al.* Iowa State U.), and the magnetic structure of $TbNi_2Ge_2$ by A.H.M. Islam *et al.* (Iowa State U.).

Spin- and Angle-Resolved Photoemission

FY 1996 was a very active year for the spin-resolved undulator beamline U5UA. Just prior to this replacement, the Magnetic Thin Films group from ANL (D. Li, J. Pearson and, S. Bader) joined the NSLS R&D group (E. Vescovo) and the BNL Physics Department's Surface Physics group (D.J. Huang, and P.D. Johnson) to perform a very challenging experiment. The goal was to elucidate the electronic states responsible for the magnetic coupling in the Cr/Fe giant magnetoresistance (GMR) materials.

Over the past few years, spin-resolved photoemission, notably the work done at U5UA, has been successful in identifying the electronic states which drive the magnetic coupling in the noble-metal based GMR materials. In this "simple" case, the long-range magnetic coupling is transmitted through the *noble-metal* spacer material via the formation of discrete, *sp*-derived, quantum-well-states (QWS). The spin of these states is determined by the spin-polarized boundary conditions at the adjacent ferromagnetic layers. The QW-like thickness dependence of these states accounts for the oscillatory behavior observed in the magnetic coupling as a function of the separation between consecutive magnetic layers.

The experiment on the atomically flat Cr/Fe(100)

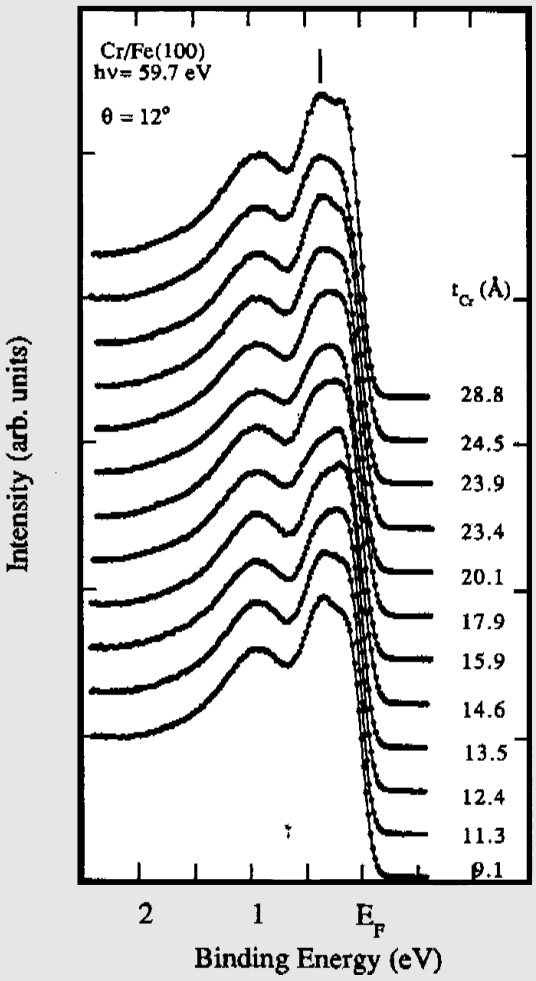

Figure 29: Photoemission spectra of Cr/Fe (100). (U5UA)

whisker was designed to attack the considerably more complex situation in which the spacer layer material is not a noble-metal: Cr has 3*d* states at the Fermi level (E_F). The QW model is hard pressed to predict the correct magnetic coupling in this case. An essential ingredient of this picture is the highly delocalized nature of the electronic states which characterize the Fermi surface of a noble metal. In the Cr case, an analysis of the bulk Cr Fermi surface suggests different pieces of the Brillouin zone as most likely to be active. Then, using angle-resolved photoemission, a careful investigation of the evolution of the photoemission spectra vs. the thickness of the Cr layer deposited on the Fe(001) whisker was conducted at these various "hot" k-points. The main result is the unambiguous identification of a 17± 2 Å oscillation period in the intensity at E_F of the energy distribution curves collected at 12° off-normal with 59.7 eV photon energy (Figure 29). This observed periodicity is in full agreement with the long-period magnetic oscillations (18 Å) found in Cr/Fe(001) multilayers. Furthermore, the "hot" k-points are in the vicinity of the d-derived "lens" feature of the Cr Fermi surface. The observation of QW-like behavior there suggests the "lens" region as the k-space origin of the long period oscillation in Fe/Cr multilayers.

Near the end of FY 1996, significant new results were obtained by a collaboration between the NYU spin-resolved group (B. Sinkovic, W. Zhu) and the NSLS R&D group (E. Vescovo) on an important magnetic materials problem of both fundamental and applied interest: half-metallic systems. The novelty of this entirely new class of magnetic materials, which was predicted theoretically a few years ago, lies in the fact that their spin-dependent electronic structure is metallic in one spin and semiconducting ~ 0.5 eV band gap in the other. Experimental evidence has so far been limited, possibly as a consequence of the considerable difficulties involved in preparing high quality surfaces of these intermetallic samples. Spin-integrated photoemission measurements from bulk single crystals have been made, which could not address the question of half-metallic character owing to lack of spin sensitivity. Recently, J.S. Moodera and coworkers from MIT have been able to prepare high quality magnetic thin films grown on various substrates, which are ideally suited for investigation by spin-resolved photoemission.

Spin-resolved measurements at the U5UA beamline were performed on a set of thin NiMnSb films (~600 Å thick) grown *ex situ* on glass and Si(001). Although *in situ* magneto-optical Kerr effect measurements indicate high magnetic remanence for these films, the measured spin-polarization of the photoemitted electrons has been found to be quite modest. In particular, the polarization of the electrons close to the Fermi level is found to be only ~20%, in contrast to the prediction of half-metallic behavior (100% polarization at E_F). Encouragingly, however, the spin-resolved photoemission measurements (Figure 30) show NiMnSb spin-resolved density of states features in good agreement with recent linear muffin tin orbital calculations. Considering the very high surface sensitivity of the photoemission measurements, these results strongly suggest that the origin of the discrepancy lies in a lowered remanent magnetization of the surface region. The next step will be to search for surface preparation methods which increase the surface remanence. Success would have great technological implications for the magnetics industry, for which the possibility of using materials with large single-spin electric carriers is often seen as a necessary prerequisite to engineer a variety of new magnetic devices.

Structural Studies of Novel Materials

The NSLS has a long history of being able to provide important characterization of new materials as they are produced, and the current year is no exception.

One newly synthesized material for which synchrotron x-ray diffraction has been important is periodic arrays of Au nanocrystals of 50-500 atoms, passivated by

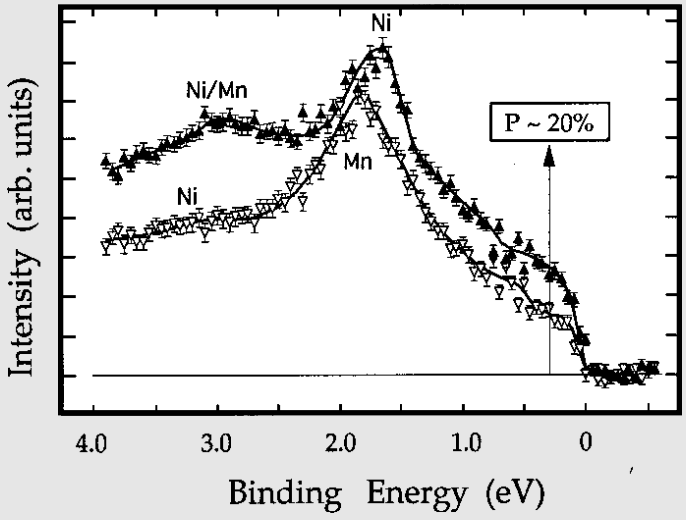

Figure 30 : Spin-resolved photoemission spectra from thin NiMnSb films at 35eV photon energy. (U5UA)

self-assembled monolayers of alkylthiolate molecules. R. Whetten *et al.* (Georgia Institute of Technology and SUNY @ Stony Brook) have developed techniques to separate fractions containing controlled shapes and sizes of the Au nanocrystals, and these materials show a very interesting diffraction pattern (Figure 31).

Another colloidal crystal system, studied by G. Beaucage *et al.* (U. of Cincinnati) on X23A3 this year, has a much larger length scale: silica in a polymer matrix with lattice parameters in the range of several μm permit an interesting opportunity to compare x-ray measurements with optical and scanning electron microscopy. This experiment makes use of the Ultra-SAXS Bonse-Hart apparatus at this beamline.

A completely different technique was applied by T. Gog *et al.* (Argonne National Laboratory) on the wiggler beamline X25 to study 50 Å GaP clusters imbedded in a Si matrix. In this work, they extended their variable energy x-ray holography technique to dilute samples, in which the lattice match between the clusters and the matrix would have made conventional x-ray diffraction analysis quite difficult.

Fullerene materials continue to generate interest, and there are several important new results from powder diffraction measurements. G. Bendele and co-workers (SUNY @ Stony Brook, X3B1) have shown that the quenched dimer phase of RbC_{60} has a different interfullerene bonding pattern than the polymeric chains found in stable RbC_{60}; a single bond between one C atom on each buckyball instead of a [2+2] cycloaddition. If one is sufficiently patient, Na_2RbC_{60} spontaneously transforms from its high-temperature cubic phase to an orthorhombic structure; previously it was thought that this transformation required the application of pressure. Incidentally, this work also showed that the orthorhombic polymer phase is not a superconductor, in contrast to what had been previously thought by some authors. M. Stetzer *et al.* (U. of Pennsylvania), have continued their investigations on beamline X7A of fullerenes with handles, viz. $C_{61}H_2$ and $C_{63}H_6$, finding two thermal phase transitions of the former and a likely unit cell for the latter.

Sliding charge-density waves exist in certain substances, and J. Brock and his colleagues at Cornell U. have made measurements using X25 to elucidate both their structure and dynamics. They have been able to provide strong evidence against recent theoretical models, which predict that the equal time phase-phase correlation function should be algebraic at large distances. Similarly, their time-resolved measurements of the decay from sliding to pinned states contradict the theoretical conclusions.

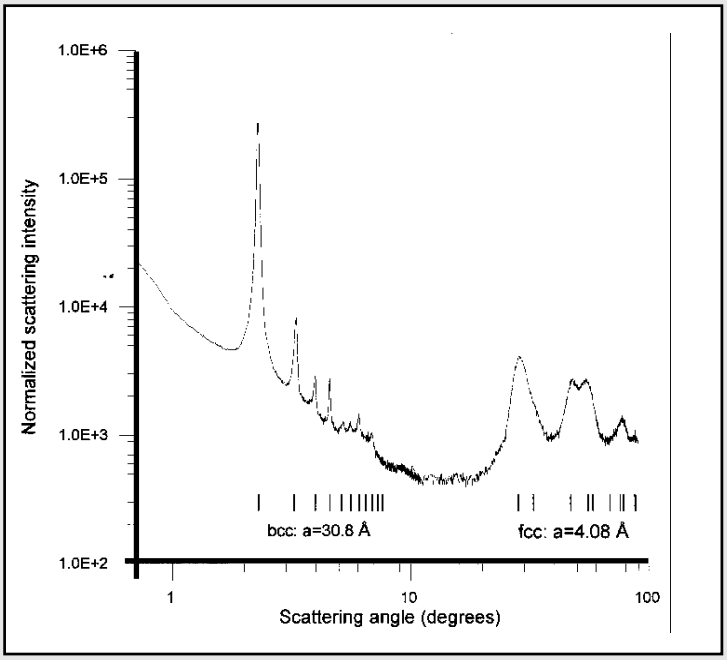

Figure 31: X-ray diffraction pattern of a bcc crystal of Au nanocrystals. The low angle peaks arise from the crystalline periodicity of a ≈ 40 Å between nanoclusters, while the spectrum at higher angles reflects the packing of Au atoms in each nanocrystal. (X3B1)

Highly Correlated Systems

Far Infrared Ellipsometry

The technique of far infrared ellipsometry is being developed by a group from the Max Planck Institute (Stuttgart, FRG) at beamline U4IR. Ellipsometry is a method for directly extracting a material's optical constants, such as the frequency dependent conductivity and dielectric function, from reflectance measurements (as a function of polarization angle for non-normal incidence). The high-brightness synchrotron infrared source makes the technique practical, as sample sizes are often very small (less than 1mm by 1 mm) and the angle of incidence must be restricted to achieve accurate results. R. Henn (Max Planck Institute) and coworkers are using this technique to investigate the c-axis infrared response of $La_{2-x}Sr_xCu_4$ for various values of x. They observe that the conductivity along this direction changes character as the Sr fraction passes through x=0.15 (which yields the optimal T_c), consistent with dc transport measurements.

X-Ray Scattering

The recent discovery of colossal magnetoresistance behavior in the perovskite-derived manganite system $La_{1-x}Ca_xMnO_3$ has stimulated much interest in the structural properties of these materials. A high resolution powder diffraction study by P.G. Radaelli *et al.* (Institut Laue Langevin), at X7A in the temperature range 20-300 K has revealed the presence of weak satellite peaks below the antiferromagnetic transition at ~180 K associated with a transverse modulation (0.5- ,0,0), corresponding to an approximate doubling of the orthorhombic a axis. The satellite intensities are consistent with charge-ordering of Mn^{3+} and Mn^{4+} ions and orbital ordering of the Jahn-Teller-distorted $Mn^{3+}O_6$ octahedra, resulting in a monoclinic structure in which the $Mn^{4+}O_6$ octahedra and one-half of the La atoms are shifted by ~0.1 and 0.05 Å respectively as indicated in Figure 32. Since then, D. Cox *et al.* (Brookhaven National Laboratory), have studied the pyrochlore $Tl_2Mn_2O_7$, and found that it does not have any lattice anomaly at the metal-insulator transition.

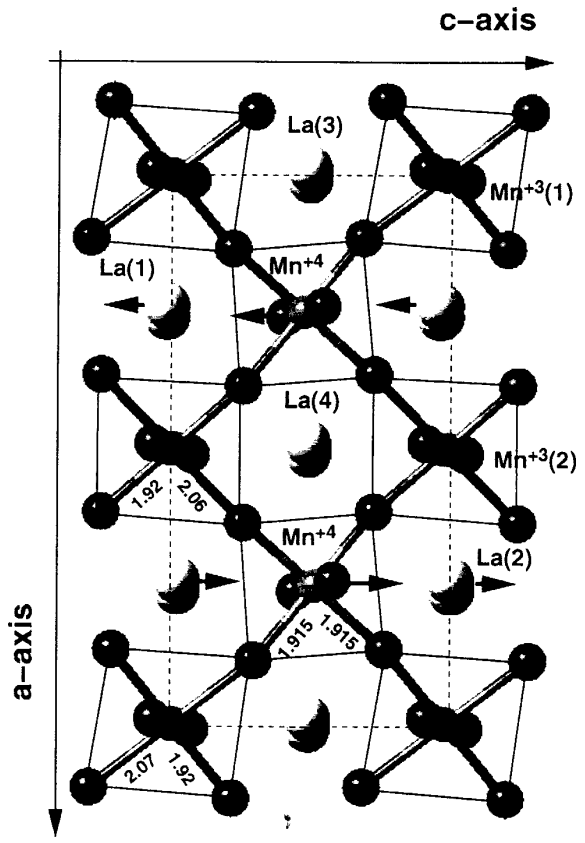

Figure 32: Structural distortions associated with the magnetic transition in $La_{0.5}Ca_{0.5}MnO_3$. (X7A)

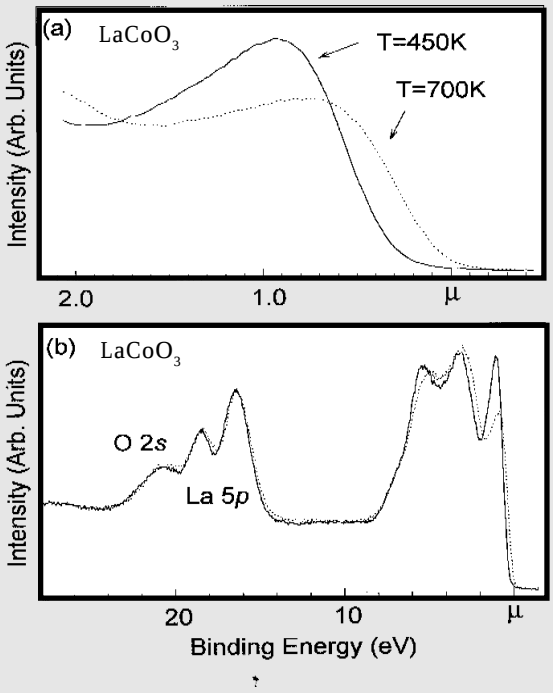

Figure 33: High resolution valence band PES spectra above (700K) and below (450K) the metal-insulator transition temperature T_t ~ 500K in $LaCoO_3$. (U4B)

X-rays are not merely a passive probe in some experiments on GMR materials. V. Kiryukhin *et al.* (Princeton U.), noted an x-ray photoinduced transition from insulating to metallic phases in $Pr_{0.7}Ca_{0.3}MnO_3$ on beamline X22B.

High-Resolution Photoemission

J.-H. Park (NSLS), S-W. Cheong (Bell Labs.) and C.T. Chen (SRRC) have investigated the high temperature metal-insulator transition of $LaCoO_3$ utilizing a high resolution valence band photoemission spectroscopy (PES) at beamline U4B. $LaCoO_3$, which exhibits a diamagnetic to paramagnetic transition around 90 K upon heating, undergoes a gradual insulator to metal transition around 500 K upon heating. Figure 33 shows the high resolution valence band PES spectra above (700 K) and below (450 K) the transition temperature T_t ~ 500 K. Upon heating through T_t, the insulating band gap disappears [Figure 33(a)], demonstrating the occurrence of the insulator to metal transition. Furthermore, considerable differences in spectral lineshape are observed in entire valence band [Figure 33(b)] at the two temperatures. These differences indicate that the metal-insulator transition is accompanied by a symmetry change, which results in an additional spin state change.

X-Ray Spectroscopy

The impact of EXAFS and XANES in the field of superconductors was evidenced by several abstracts from beamline U4B and X11A, using soft and hard x-ray spectroscopy respectively. Oxygen K-edge NEXAFS was used to understand how oxygen orbital structure correlates with the superconductivity of the material. For example, several groups examined superconductors of the type: $(Y_zRE_{1-z})Ba_2Cu_3O_y$. Generally, rare earth substitution has little effect on the superconducting properties, with the notable exception of Pr. Oxygen 1*s* NEXAFS of superconductors with increasing concentrations of Pr were examined and showed specific changes in oxygen orbital structure consistent with the presence of Fehrenbacher-Rice states.

In another investigation on beamline X11A, D. Haskel and E. Stern (U, of Washington) investigated the structural consequences of Sr^{+2} substitution for La^{+3} in $La_{2-x}Sr_xCuO_4$. Sr^{+2} in the range of 0.075 to 0.25 leads to high T_c superconductivity by inducing hole carriers in the Cu-O planes. By examining the Sr-K edge EXAFS of oriented powders, it was shown that the Sr-O bonding structure is quite different from that of La-O bonding. In particular, the apical oxygen atoms are split into 2 sites separated by 0.3 Å (Figure 34). This implies a fluctuating number of holes at the Cu sites near the Sr atoms. The hole-lattice interaction could be involved in the pairing mechanism, leading to high T_c.

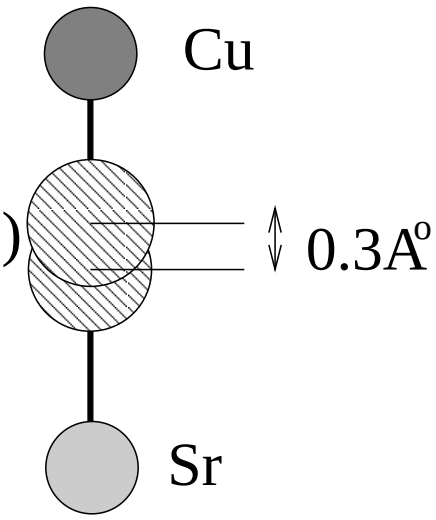

Figure 34: Two site configuration of the 0_2 apical to Sr. (X11A)

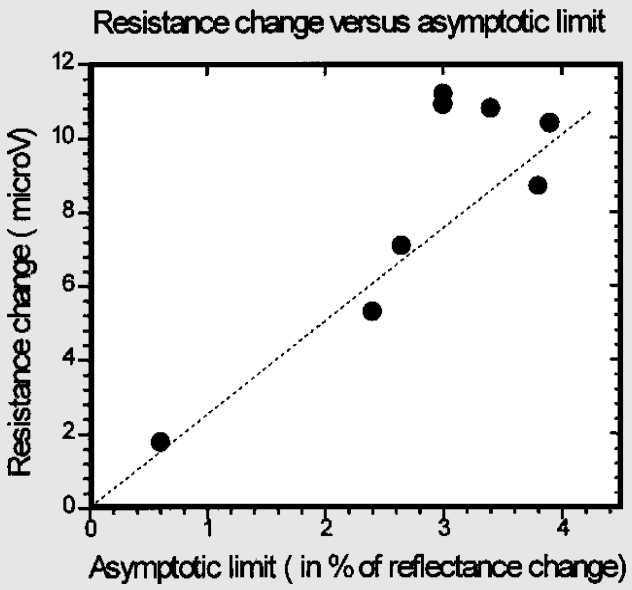

Figure 35: The change in resistance (measured as a voltage under constant current bias) of a thin Cu film versus the infrared reflectance change for 8 different coverages of CO adsorbate. (U4IR)

Surface Dynamics

The primary program at beamline U4IR continues to be studies of molecular adsorbates on metal surfaces by grazing incidence reflectance spectroscopy. Of particular interest is the broadband reflectance change of the metallic substrate as a function of the particular adsorbate and its coverage. Research groups from Duesseldorf, LURE, Tufts, the ALS and the NSLS are studying various aspects of this behavior. The theoretical model of B.N.J. Persson explains the reflectance change as due to enhanced scattering of the metal's electrons from the adsorbate. This scattering affects the surface resistance, and the theory predicts a linear relationship between the electrical surface resistance and the reflectance change. In work by M. Hein, P. Dumas, and collaborators (Duesseldorf, LURE and the NSLS), both the reflectivity change and resistivity were measured for thin Cu(111) films as a function of coverage for CO, oxygen, and ethylene adsorbates as shown in Figure 35. In accord with theory, the reflectance change for CO and ethylene was found to be linear with the resistivity change. However, the behavior for oxygen showed some departures from the model predictions.

Another adsorbate-on-metal system, namely C_{60} on various noble metals [Ag(111), Au(110), Cu(111)], was

investigated by P. Rudolf (LISE-Namur, Belgium) and coworkers from LURE (France), Lucent Technologies, and the NSLS. C_{60} readily accepts charge from alkali metals (such as potassium) to form a conducting "fulleride", which is accompanied by distinct changes in several of the C_{60} molecule's IR vibrational modes. In this study of C_{60} deposited on Ag, Au, and Cu, only one absorption mode is observed (Figure 36), assigned to the Raman active Ag(2) mode. The mode has become IR active due to symmetry breaking upon adsorption. The appearance of such a mode suggests a strong interaction between the metal and the C_{60} molecule. However, none of the fulleride modes were apparent, indicating that if charge transfer (from the metal to the C_{60} molecule) occurs, it is quite different from that associated with alkali metal doping. Pre-dosing the noble metal surface with K leads to even more interesting behaviors when C_{60} is deposited. For C_{60} on 1ML of K, the Ag(2) mode absorption appears as an anti-resonance. This is similar to what is found for CO on Cu, indicating that conduction electrons in the metal substrate must experience strong scattering from the adsorbate. Apparently some charge transfer occurs from the K onto the C_{60}, leading to a larger scattering cross section for conduction electrons near the substrate surface. A fulleride does form when C_{60} is deposited onto thicker layers of K, as witnessed by the appearance of an absorption mode at 1356 cm^{-1}. The anti-absorption mode at 1450 cm^{-1} persists.

High Pressure Research

The group from the Carnegie Institution of Washington (R. Hemley, A. Goncharov, R. Lu, H.K. Mao *et al.*) continued their investigations of dense hydrogen at beamline U2B, while expanding their program to include other compounds and minerals at extremely high pressures. Results of IR spectroscopy on hydrogen to pressures above 200 GPa have contributed to our understanding of the phase diagram for the solid. A transition from the low pressure, high temperature phase (I) to an intermediate phase (II) occurs for pressures above ~100 GPa and T<100 K. A third phase (III) is observed for pressures above 150 GPa. In phases II and III, the absorption associated with coupled vibrational modes in the molecular solid (vibrons) shifts in frequency and strength as a function of pressure and temperature (Figure 37, on next page). The oscillator strength (expressed as an effective charge) and frequency shift were found to share a common temperature dependence in both phase II and phase III. This allowed the Carnegie group to relate both quantities to an order parameter that characterizes the particular phase. This information, combined with results from Raman studies, have led to a picture where phase II consists of molecules with ordered angular momentum, and in phase III the molecules themselves are physically ordered. Thus, the high pressure phases of solid hydrogen can display quantum mechanical or classical ordering.

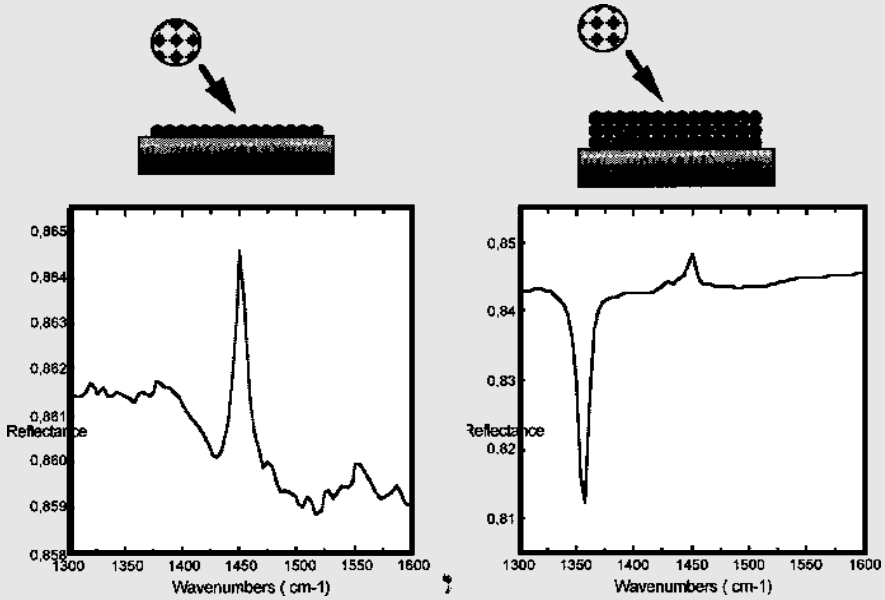

Figure 36: Reflectance from an adsorbed layer of C_{60} on a crystal of Ag which has been predosed with K. Left: a single monolayer of K on Ag precedes the C_{60} dose. Right: a thick layer of K precedes the C_{60} dose. (U4IR)

The Carnegie group have also investigated mixtures of hydrogen with other simple gases (e.g. CH_4, Ar) to high pressures. Similar to the situation for pure H, the molecular solids show IR absorption features associated with vibrational and rotational modes, but there has been no evidence of metallic behavior to the highest pressures achieved so far.

Equation of State

While P-V-T measurements have become routine in synchrotron studies over the past few years, they still provide new insights into material properties and a probe to bonding characteristics. Peiris and Heinz demonstrate the effects of vacancies in ScS on the bulk modulus. They find that the vacancies actually increase the bulk modulus, a result which they explain in terms of the changing bonding characteristics of the material. Zhang and Reeder demonstrate that the bulk modulus-volume systematics for calcite-structure carbonates is sensitive to the cation, with alkaline earth cations defining a different relationship than transition metals, suggesting differences in bonding characteristics.

Phase Equilibria

X-ray diffraction patterns serve as fingerprints for the phases that exist in the high pressure system. S. Qadri *et al*. (Naval Research Laboratory), document the effect of particle size on phase transitions of PbS and E. Skelton *et al.* (Naval Research Laboratory), examine transition rates in Pd as affected by electrochemical absorption of deuterium both on X17C. J. Hriljac *et al.* (U. of Birmingham), explore, on X7A, the phase stability fields of mercury-based superconductors.

J. Chen *et al.* (SUNY @ Stony Brook), explore the pressure induced amorphization of zironium tungstate, the interesting material with a negative thermal expansion, Q. Chen *et al.* (U. of Western Ontario) combined x-ray diffraction with electrical conductivity to study silver sulfate and various tellurium salts. These studies utilized various high pressure systems and share in common the goal to use pressure as a thermodynamic variable to map out the stability fields of a variety of novel materials. Both of these studies were carried out on X17B1.

Electronic Structure

Inelastic X-Ray Scattering

Inelastic X-Ray Scattering Spectroscopy (IXSS) is becoming a routine experimental technique in the study of electronic excitations in atomic, molecular, and condensed matter systems. It provides information complementary to photoelectron spectroscopy, optical spectroscopy, electron energy loss spectroscopy, and x-ray absorption spectroscopy. It also allows greater flexibilty in the selection of sample environment and experimental conditions.

The IXSS measurements carried out at NSLS can be divided into two categories: non-resonant Raman scattering and resonant Raman scattering. In the case of non-resonant Raman scattering, the energy of the incident x-ray is far away from that of any absorption edge of the sample. The double differential cross section is then

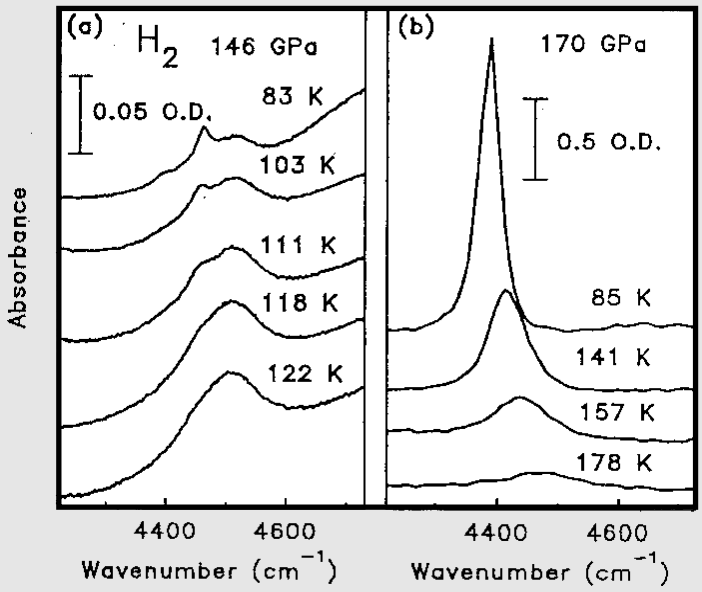

Figure 37: Absorbance measurements of H_2 at high pressures and low temperatures, showing the change in the vibron mode's frequency and strength. Left: Intermediate (angular momentum ordered) phase, Right: High pressure (classically ordered) phase. (U2B)

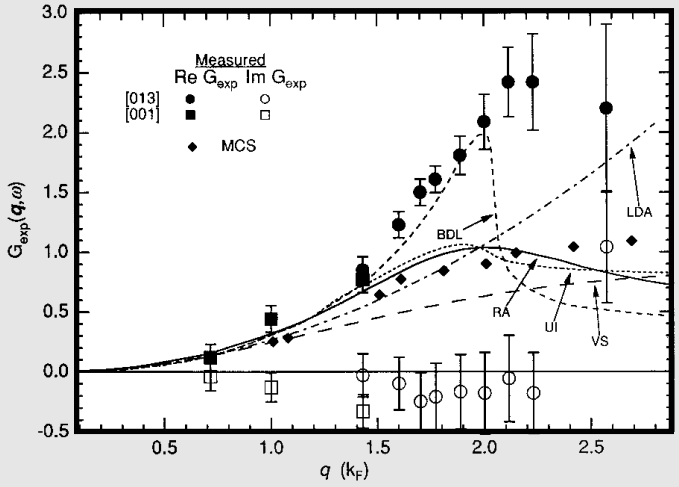

Figure 38: Comparison between experimental and theoretical local-field factors of Al metal as a function of momentum transfer. (X14A)

related directly to the dielectric response function of the system under investigation. Although electron energy loss spectroscopy (EELS) also provides the same information, it suffers from multiple scattering problem at medium to high momentum transfers. As a result, few reliable experimental results are available in these momentum transfer regimes. Another problem with EELS is that samples have to be very thin and vacuum compatible.

To take special advantage of IXSS, several groups have measured the dynamical structure factor, S(q,w), of simple metals near q = $2k_F$, where q is the momentum transfer and k_F is the Fermi momentum. The measured lineshape shows large discrepancies from the prediction of the simplest many-body theory, often referring to as the Random Phase Approximation (RPA). B. Larson (ORNL) *et al.* measured the dynamical structure factor of Al from 0.7 to 2.57 k_F, and compared them with first principle dynamical electronic response calculations to extract the local-field factors as a function of momentum transfer (Figure 38). They found that for q = $2k_F$ and larger the experimentally determined local-field factors are nearly twice as large as the calculated values; and suggested that even in simple metals dynamical electron correlations are quite strong. In a closely related experiment, J. Hill *et al.* (Brookhaven National Laboratory), following on from their earlier work on liquid Li and Na, measured the dynamical structure factors of solid and liquid Al near q = $2k_F$ to disentangle the effects of long-range order from intrinsic many-body electron-electron correlation effects. They found that the overall lineshape is very similar between the liquid and the solid; while the fine structure in the linehape for the solid phase is significantly reduced in the liquid (Figure 39). These findings suggest that the overall lineshape of the response is due to electron correlations, and that the fine structure in the solid phase is not related to many-body effects. A similar study was also extended to single crystal Na by P. Chow *et al.* (University of Houston). These and future experimental studies in combination with more first principle calculations will certainly contribute to our understanding of the many-body exchange-correlation effects in simple metals.

In the case of resonant Raman scattering, the energy of the incident x-ray is tuned near that of an absorption edge of the sample. By exploiting the resonant condition in the $\vec{A} \cdot \vec{P}$ terms of the electron-photon interaction Hamiltonian, the inelastic scattering cross section can be greatly enhanced. The wider tuneability of the new X21 monochromator was designed so that the K edges of the late 3*d* metals and the L edges of all of the rare earth elements can be easily

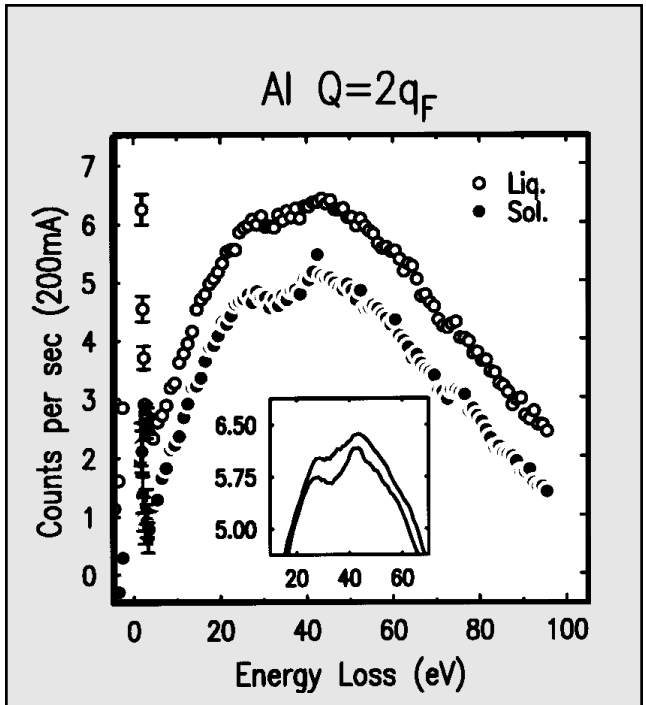

Figure 39: Dynamical structure factors of solid Al versus liquid Al near momentum transfer $2k_F$.(X21)

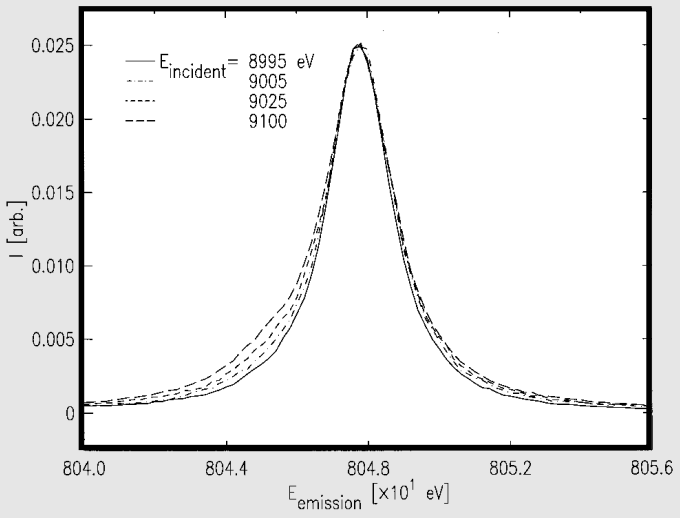

Figure 40: Cu K-α emission spectra as a function of incident photon energy from Cu. (X21)

covered to facilitate this class of experiment. Resonant Raman experiments conducted near the K edges of Mn, Fe, Ni, and Cu were reported this year.

Continuing their study of many electron excitations near the K edge threshold of 3*d* metals, M. Deutsch *et al.* (Bar-Ilan U.) studied the near-threshold behavior of the Cu K-$\alpha_{1,2}$ emission lines. Three regimes were identified: (1) For incident energies below 8981 eV, the energies of K-$\alpha_{1,2}$ emission lines show linear dispersion with incident photon energy, and the intensities of the emission lines show rapid decrease with decreasing incident photon energy. Both are characteristic behavior of resonant Raman scattering below an absorption threshold. (2) For incident energies between 8981 eV and 8995 eV, the lineshape is purely Lorentzian indicating that the 3*d* spectator transitions are still energetically forbidden within this energy range. (3) For incident energies above 9000 eV, 3*d* spectator transitions become energetically allowed. As shown in Figure 40, the contributions from the spectator transitions are most pronounced on the low-energy side of the K-α_1 emission line. Lineshape analysis is used to extract the evolution of the strength of the 3*d* spectator transitions with incident photon energy, which is important in the understanding of electron-electron correlation in these systems.

A common feature in the K edge x-ray absorption spectra of 3*d* transition metal compounds is a weak pre-edge peak below the absorption threshold. It is typically assigned to $1s \rightarrow 3d$ transition. The strength of the transition depends on the symmetry of the local environment around the transition metal. With 0.2 eV incident energy resolution, the splitting of the pre-edge feature due to the crystal-field can be resolved in some cases. In resonant Raman scattering experiments, one can then selectively excite the 1*s* electron to one of the crystal-field split states, and monitor the decay of the core hole through either $2p \rightarrow 1s$ emission channel or $3p \rightarrow 1s$ emission channel. The final state of the resonant Raman process then becomes either $2p^5 3d^{n+1}$ or $3p^5 3d^{n+1}$, the same final state configurations reached by either $L_{2,3}$ edge or $M_{2,3}$ edge soft-x-ray absorption processes. As a result, the rich $L_{2,3}$ edge many-electron multiplet structure can be obtained at the K edge x-ray energies, a combination that is very important in cases where samples are not vacuum compatible. An example was given by W. Caliebe *et al.* (U. of Kiel), in a high resolution resonant Raman scattering study of Fe_2O_3, -hematite at the Fe K edge. Figure 41 shows the two Raman spectra taken at incident x-ray energy tuned to the two crystal-field split states. Notice that it is the final state energies that are plotted. Also shown in the figure is the Fe $L_{2,3}$ edge absorption spectrum. Clearly, the energies of the two

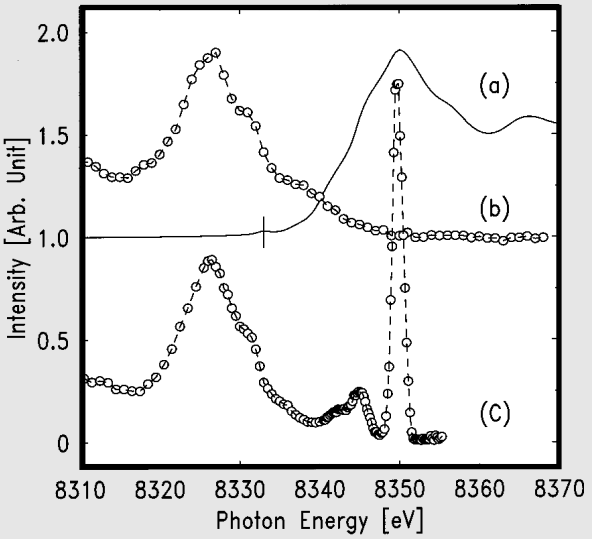

Figure 41: (a) Fe $L_{2,3}$ absorption spectrum of Fe_2O_3; (b) Resonant Raman spectrum from Fe_2O_3 obtained with incident photon energy tuned to 7113.4 eV (t2g symmetry); (c) Resonant Raman spectrum from Fe_2O_3 obtained with incident photon energy tuned to 7114.8 eV (e.g. symmetry). (X21)

main features in the soft-x-ray absorption spectrum agree very well with the main peak in the two Raman spectra.

Large resonant enhancement of valence electron excitations was also observed. C.-C. Kao *et al.* (Brookhaven National Laboratory) reported a high resolution resonant Raman scattering study of NiO, a prototypical Mott-Hubbard system. As the incident photon energy is tuned through the Ni K edge, a new loss feature, which is not observed for incident energies far from the absorption edge, is observed. Figure 42 shows the Ni K absorption spectrum of NiO (a), the valence band emission spectrum of NiO (b), and the Raman spectrum taken with the incident energy tuned to the peak of the white line in the absorption spectrum (c). The new loss feature can be roughly fit with two peaks centered around 5 eV and 8 eV. These observations were interpreted by using a configuration interaction cluster model, and the new loss feature is identified as the charge transfer excitation in NiO. Subsequently, resonant enhancement of charge transfer excitations near the K edge of Cu have been observed by Hill *et al.* in Nd_2CuO_4, and by Isaacs *et al.* in $Sr_2CuO_2Cl_2$.

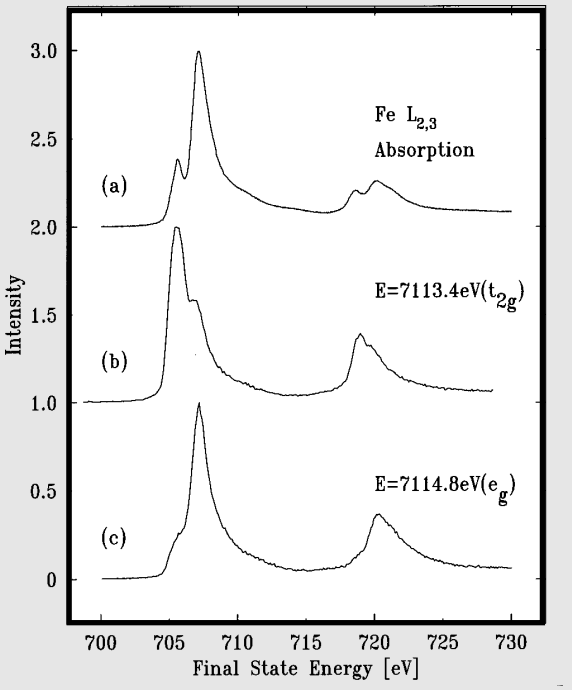

Figure 42: (a) Ni K absorption spectrum of NiO; (b) Normal valence band x-ray emission spectrum of NiO; (c) Resonant inelastic x-ray scattering spectrum of NiO obtained with the incident photon energy tuned to the main peak of the absorption spectrum (a). (X21)

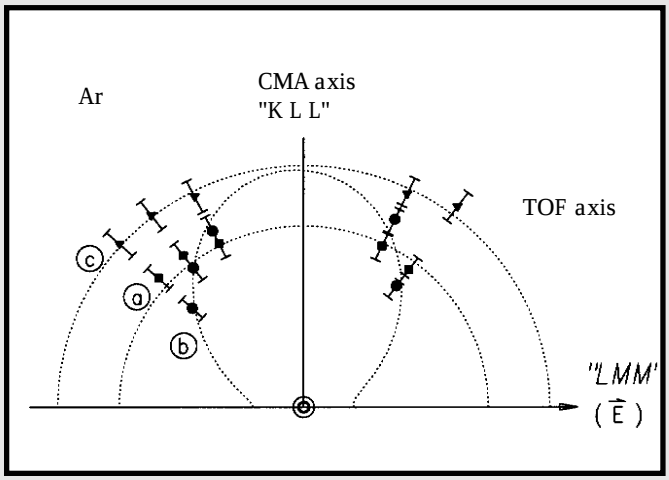

Figure 43: Auger-Auger electron coincidence measurement from Ar gas excited at the 1s → 4p resonance (3203.5eV). Polar plot showing the angular correlation between three slices (a, b, and c) of the LMM Auger group and the $KL_{2,3}L_{2,3}$ Auger electrons. (X24A)

In summary, the examples highlighted above are a good demonstration of the versatility of IXSS as a probe of electronic excitations in a wide range of systems.

Core Excitation

An Auger-Auger electron coincidence experiment at beamline X24A has been able to detect a large non-isotropic angular correlation between different components of the well-known Auger electron cascade following the 1s → 4p resonant excitation of Ar gas. One electron detector, a time-of-flight (TOF) spectrometer, was set to collect large portions of the LMM Auger envelope while the other, a cylindrical mirror analyzer (CMA) equipped with multichannel detection in order to determine the polar and azimuthal angles, was set to collect the precursor $KL_{2,3}L_{2,3}$ Auger electrons. The TOF spectrometer was oriented along the electric field vector of the monochromatized synchrotron radiation and the CMA was aligned perpendicular to both the TOF axis and the photon beam direction. Operation of the TOF spectrometer requires single-bunch operation of the X-Ray Ring in order to avoid overlapping signals from adjacent electron bunches.

By dividing the LMM Auger envelope into three slices, a large non-isotropic angular correlation was observed for one of these slices (Figure 43), whereas the others were isotropic. The large anisotropy observed is believed to be an alignment effect rather than a dynamical post-collision interaction effect.

Angle-Resolved Photoemission

The first results of a program and experimental chamber dedicated to high resolution (in angle and electron energy) angle-resolved photoemission were obtained at the end of FY 1996 by E. Jensen, T. Balasubramanian (Brandeis U.), X. Wu and S. Hulbert (NSLS) at beamline U12B. This first experiment was a study of the electronic structure of the (0001) surface of beryllium (Be) near the Fermi level (E_F). The electronic density of states (DOS) at the Fermi level of the Be(0001) surface is about four times larger than in the bulk. Many properties such as the electron-phonon interaction, the resistivity, and the specific heat depend strongly on the DOS at E_F. In particular, the electron-phonon coupling parameter λ is directly proportional to the DOS at E_F.

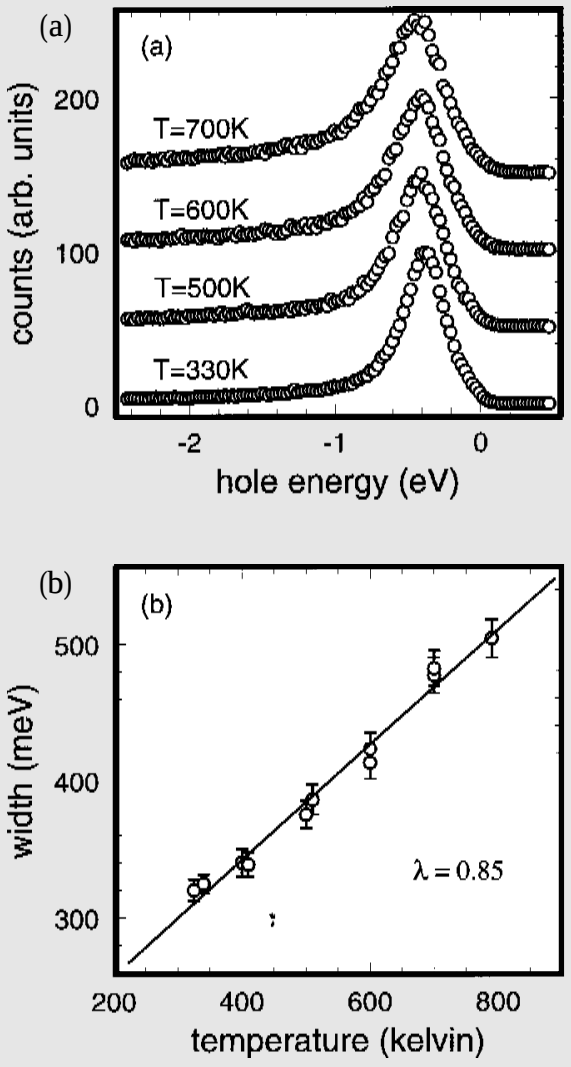

Figure 44: (a) Be(0001) $\overline{\Gamma}-\overline{K}$ surface state at various temperatures. The momentum is 0.93 Å^{-1}, the hole energy is 0.4 eV and the photon energy is 15 eV. (b). Width of the surface state peak vs. temperature. Circles with error bars are experimental data, line is a fit yielding λ=0.85. (U12B)

For bulk Be, λ is 0.24. Thus one would expect the surface λ to be about unity. λ was measured at the Be(0001) surface using angle resolved photoemission. The full width at half maximum (fwhm) of the surface state (SS) is interpeted as the inverse hole life time. All of the temperature dependence of the lifetime at high temperature comes from the phonon contribution, which is given by $2\pi\lambda kT$. Thus by measuring the SS fwhm vs. temperature one can determine λ. The $\overline{\Gamma}-\overline{K}$ SS, one of three on the Be(0001) surface, was chosen for measurement. This state has a binding energy of 2.8 eV at $\overline{\Gamma}$ and disperses parabolically, crossing E_F at $k_{||}$ =0.95 Å^{-1}. Figure 44(a) shows photoemission from this SS at $k_{||}$ =0.93 Å^{-1} (0.4 eV hole energy) for several temperatures. The fwhm of the SS is plotted vs. temperature in Figure 44(b). Fitting these data to a straight line yields λ=0.85 $\pm$ 0.1.

Using λ=0.85 in the standard formula relating λ to a superconducting transition temperature T_c, one finds that T_c rises to about 50 K (from 0.026 K in the bulk). This should be observable in ultra-thin films, and may have observable consequences for the surface of a thick crystal at low temperatures.

The success of this experiment was determined in large part by the ability to prepare an extremely clean Be(0001) surface, an exercise which required more than one calendar year of effort. During FY 1997, an effort will be made to determine the electron-electron and electron-impurity contributions to the Be(0001) SS lifetime. Also, a new high-resolution angle-resolved photoemission analyzer and experimental endstation, funded by the DOE Scientific Facilities Initiative, are being fabricated.

Significant progress has been made recently by S. Dhesi, C. Stagarescu, and K. Smith (Boston U.) in the study of the electronic structure of wide band gap nitride semiconductors. Such semiconductors (for example, GaN) are an important class electronic materials primarily due to potential use in optoelectronic devices operating in the blue to ultraviolet spectral range. Using angle-resolved photoemission on beamline U4A, the band dispersion of the valence states along all the high symmetry directions in the bulk Brillouin zone has been measured for wurtzite GaN thin films. The n-type wurtzite GaN(001) thin films were grown using electron cyclotron resonance assisted molecular beam epitaxy on sapphire substrates at Clean GaN(0001) surfaces were prepared by repeated cycles of N_2^+ sputtering and

annealing in UHV. Following this procedure Auger electron spectroscopy shows minimal contamination, and low energy electron diffraction displays a sharp hexagonal pattern with no evidence of a surface reconstruction.

Figure 45 shows a series of normal emission spectra taken from atomically clean GaN(0001) surface of a wurtzite film. The spectra in Figure 49 reflect the dispersion of the states along the ΓAΓ direction of the bulk Brillouin zone. By measuring spectra in the off-normal geometry, the dispersion of states along directions in the bulk Brillouin zone parallel to the surface were also measured. The results of these experiments reveal very good agreement with local density approximation calculations for the bulk band structure. One notable result of the angle resolved photoemission measurements is the observation of a non-dispersive surface state about the $\overline{K}$ point in the surface Brillouin zone. This state exists in a projected bulk band gap, and is sensitive to oxygen adsorption.

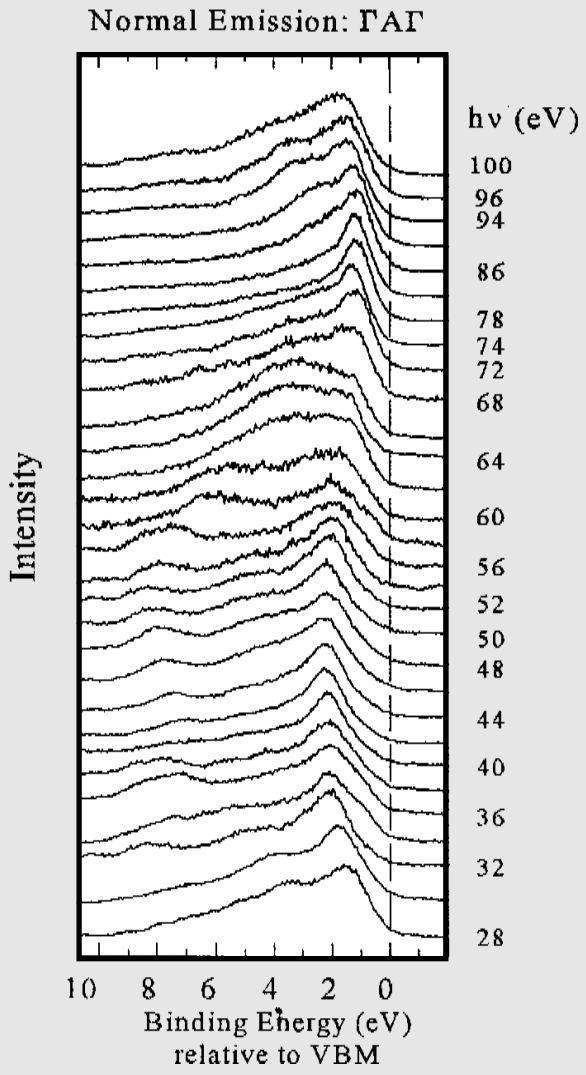

Figure 45: Angle resolved photoemission spectra taken at normal emission from atomically clean GaN(0001) surface of a wurtzite film. These spectra reflect the dispersion of the states along the ΓAΓ direction of the bulk Brillouin zone. (U4A)

Auger Photoelectron Coincidence Spectroscopy (APECS)

The Auger Photoelectron Coincidence Spectroscopy endstation continues to utilize its unique capabilities to study interesting surface science phenomena. During FY 1996, two APECS experiments were performed at beamline U14A.

In one of these, the $N_{2,3}VV$ Auger spectra from the Ru(0001) surface taken in time coincidence with Ru $4p_{3/2}$ or $4p_{1/2}$ core photoelectrons are compared. As would be expected for highly correlated late transition metals such as Ru, the measured APECS Auger spectra are not well represented by the self-convolution of the Ru(0001) valence band density of states. On the other hand, an attempt to model the Auger spectra by multiplets of a d^6 configuration, appropriate if the 4p core hole is fully screened prior to Auger decay, has met with some success: the differences between the two experimental spectra can be explained by a stronger coupling of the high kinetic energy ^5D multiplet term to the $4p_{3/2}$ level than the $4p_{1/2}$ level. Calculation of the appropriate matrix elements is underway. This experiment is the result of a collaboration between R. Bartynski and R. Gotter (Rutgers U.), X. Wu and S. Hulbert (NSLS), and H. Nozoye (Japan National Institute of Materials and Chemical Research).

The second APECS experiment of FY 1996, also performed at U14A, has put the finishing touches on a set of APECS measurements of the lineshape of the Ti 3*p* core level spectrum from stoichiometric ("nearly perfect") and defective TiO_2(110) surfaces, measured in time coincidence with $M_{2,3}VV$ Auger electrons. The selection of only those Ti 3*p* core holes which decay by $M_{2,3}VV$ Auger emission provides a new spectroscopic view of this surface. Figure 46 (a),(b), and (c) (see next page) show coincidence Ti 3*p* core level spectra from the stoichiometric, 900 K vacuum annealed, and ion bombarded (~10^{14} Ar^+ ions/cm^2 at 500eV) surfaces, respectively. Figure 46 (d), (e), and (f) show non-coincidence (ordinary, or "singles") spectra from the same three surfaces. The excess emission in the 68-70eV kinetic energy range in Figure 50(a) is attributed to Ti^{3+} and Ti^{2+} ions in sites

adjacent to surface oxygen vacancies. The density of these residual surface defects (either point defects or step edges) is rather low (~1% of a monolayer) on the stoichiometric surface, but the associated sub-oxide emission accounts for ~20% of the total surface Ti 3*p* emission [Figure 46(a)]. The enhanced sensitivity in the coincidence spectrum is attributed to the extra charge density at the reduced Ti sites as compared to Ti^{4+} sites, which strongly affects the $M_{2,3}VV$ Auger decay rate. The assignment of this excess emission as defect- related is supported by the spectra in Figure 46(b) and (e). 900 K annealing induces only a small (~4%) defect-related shoulder in the singles spectrum [Figure 46(b)] while in the coincidence spectrum [Figure 46(e)] over 50% of the Ti 3*p* emission is associated with reduced Ti oxidation states. Ion bombardment produces a greater fraction of defect-related emission in the singles spectrum [Figure 46(f)] than does 900 K annealing [Figure 46(e)], but results in a very similar coincidence spectrum. This shows that this ion dose produces a concentration of surface defects similar to what 900 K annealing produces, and that a substantial fraction of the defect-related emission in the singles spectra arises from subsurface damage.

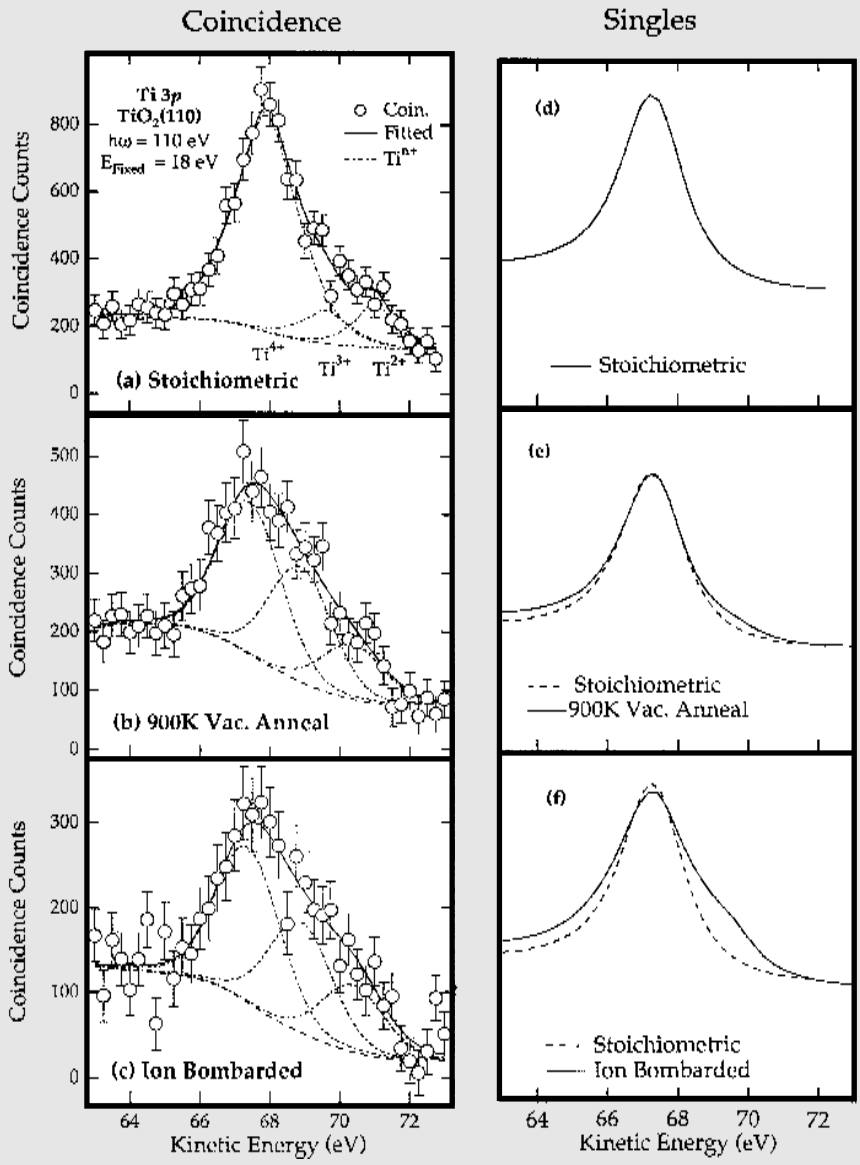

Figure 46: A series of Ti 3p core level photoemission spectra from TiO_2(110) taken at 110eV photon energy, both with (a-c) and without (d-f) the requirement of time coincidence with $M_{2,3}VV$ Auger electron emission. Surface treatments: (a),(d): nearly-perfect stoichiometric surface; (b),(e): after 900K vacuum anneal; (c),(f): after ion bombardment. (U14A)